

Effects of $(\text{Mg}_{1/3}\text{Sb}_{2/3})^{4+}$ substitution on the structure and microwave dielectric properties of $\text{Ce}_2\text{Zr}_{3x}(\text{Mg}_{1/3}\text{Sb}_{2/3})_{3-3x}(\text{MoO}_4)_9$ ceramics

Xu ZHOU^a, Jiajia SUN^a, Ningkang ZHANG^a, Huazhang SUN^a, Wenhong TAO^{a,*}, Haitao WU^{b,*}

^a School of Materials Science and Engineering, University of Jinan, Jinan, 250022, Shandong, China

^b School of Environmental and Material Engineering, Yantai University, Yantai, 264005, Shandong, China

Abstract

$\text{Ce}_2[\text{Zr}_{1-x}(\text{Mg}_{1/3}\text{Sb}_{2/3})_x]_3(\text{MoO}_4)_9$ ($0.02 \leq x \leq 0.10$) ceramics were prepared well through the traditional solid-state method. A single phase, belonging to the space group of R-3c, was detected by using X-ray diffraction at sintering temperatures ranging from 700 to 850 °C. The crystallization micro-structural of specimens was examined by applying Scanning electron microscopy. The structural refinement of these samples was investigated in detail by performing the Rietveld refinement method. The intrinsic properties were calculated and explored via far-infrared reflectivity spectroscopy. The correlations between the chemical bonds parameters and microwave dielectric properties were calculated and analyzed by P-V-L theory. $\text{Ce}_2[\text{Zr}_{0.94}(\text{Mg}_{1/3}\text{Sb}_{2/3})_{0.06}]_3(\text{MoO}_4)_9$ ceramics with excellent dielectric properties: $\epsilon_r = 10.37$, $Q \times f = 71748$ GHz and $\tau_f = -13.6$ ppm/°C sintered at 725 °C for 6 hours.

Keywords: structure; P-V-L theory; microwave dielectric property; $(\text{Mg}_{1/3}\text{Sb}_{2/3})$ doping

1. Introduction

It is well-known that dielectric materials have developed rapidly in the past decades. Microwave dielectric ceramics have sprung up in the communication industry and received widely attention. It is required to have a high quality factor ($Q \times f$), a moderate dielectric constant (ϵ_r) and a near-zero temperature coefficient of resonant frequency (τ_f) to meet the demands of application [1-4]. Recently, researchers focused on novel microwave dielectric ceramics [5-7]. At the same time, some researchers have been widely investigated the substitution of cationic and composite ceramics to improve the dielectric properties of microwave dielectric materials [8-12]. In addition, high cost limits the application of these ceramics, and consequently it is required to reduce their sintering temperature. The low

*Corresponding author. Haitao Wu, mse_wuht@ujn.edu.cn

temperature co-fired ceramic (LTCC) [13-18] technology has become a common method due to its simplicity and high efficiency. Hence, LTCC technology is becoming more and more important in practical application.

In recent years, $A_2Zr_3(MoO_4)_9$ (A=Sm, Nd, Eu, and Ce, etc.) microwave dielectric ceramics have been studied in depth [19,20]. Many microwave dielectric ceramic systems have been developed, but their properties are not optimistic. The performance ($Q \times f = 19062$ GHz) of $Ce_2Zr_3(MoO_4)_9$ ceramic was investigated [21]. In order to improve the better selectivity of $Ce_2Zr_3(MoO_4)_9$ ceramics, doping $(Mg_{1/3}Sb_{2/3})^{4+}$ at Zr-sites was reported in this work. The crystal structure and sintering behavior of samples was discussed in detail. Also, relationship between the dielectric properties and structure of samples was explored scientifically by far infrared (IR) reflectivity spectrum and the P-V-L theory.

2. Experimental procedure

Highly pure powders of CeO_2 , ZrO_2 , MoO_3 , MgO and Sb_2O_5 were weighed accurately based on the stoichiometric composition of $Ce_2[Zr_{1-x}(Mg_{1/3}Sb_{2/3})_x]_3(MoO_4)_9$ ($0.02 \leq x \leq 0.10$). The mixed powders were continuously rotated for 24 h with ethanol media and ZrO_2 balls. Mixtures were oven-dried at 80 °C and pre-sintered at 700 °C for 2 h. After that, ball milled and dried again under the same condition as above. Subsequently, the combination of powders and 10 wt% paraffin passed through a 60 mesh sieve, and a certain size of the cylinders (length ~ 6 mm, diameter ~ 10 mm) was pressed at 200 MPa. Those pressed cylinders were sintered from 700 to 850 °C for 6 h.

Phase identification of sintered pellets were analyzed using X-ray diffraction (D8 Advance, Bruker Co., Germany) with Cu $K\alpha$ radiation and refined lattice parameters were obtained using FULLPROF program to explore structure. The surface microstructures of specimens were observed by scanning electron microscopy (SEM: FEI Co., United States), equipped with EDS. The apparent densities of specimens were analyzed using Archimedes method. The infrared reflectivity spectrum was recorded by a Bruker IFS66v FTIR spectrometer. In addition, dielectric behaviors were surveyed by employing the TE_{018} cavity method with a network analyzer (N5234A, Agilent Co., USA) and the Hakki-Coleman dielectric resonator method. The τ_f value was acquired by formula (1):

$$\tau_f = \frac{f_r - f_0}{60 \times f_0} \times 10^6 \text{ (ppm / } ^\circ\text{C)} \quad (1)$$

where, f_T and f_0 represent resonant frequencies at 85 °C and 25 °C, respectively.

Relative density ($\rho_{relative}$) was applied via the following formula (2)-(3):

$$\rho_{theory} = \frac{ZA}{V_c N_A} (g / cm^3) \quad (2)$$

$$\rho_{relative} = \frac{\rho_{apparent}}{\rho_{theory}} \times 100\% \quad (3)$$

where Z is the number of molecules, N_A refer to Avogadro constant, V_C represent unit cell volume.

3. Results and discussion

As shown in Fig. 1, the X-ray diffraction patterns of $Ce_2[Zr_{1-x}(Mg_{1/3}Sb_{2/3})_x]_3(MoO_4)_9$ ($0.02 \leq x \leq 0.10$) ceramics sintered under different temperatures for 6 h. A single phase was detected in all samples. The peaks of sintered ceramics assigned to the standard data for $Pr_2Zr_3(MoO_4)_9$ (JCPDS No. 52-0688), which indicated that the $Pr_2Zr_3(MoO_4)_9$ -like crystal structure with a R-3c space group was obtained. According to the result, the composition of the crystal phase is not changed by the content of $(Mg_{1/3}Sb_{2/3})^{4+}$ ions substitution [22]. In order to meet the needs of calculating density and complex chemical bonds to further analyze its structure, lattice parameters, bond length and unit cell volumes were obtained by Rietveld refinement [23]. $Nd_2Zr_3(MoO_4)_9$ was chosen as the original model via FULLPROF program. Refinement plot of $Ce_2[Zr_{1-x}(Mg_{1/3}Sb_{2/3})_x]_3(MoO_4)_9$ ($0.02 \leq x \leq 0.10$) ceramics were displayed in Fig. 2, in which the observed values were expressed by red points, the calculated values were expressed by the black line, and the difference value between the observed and the calculated data expressed by the blue curve. Obviously, excellent agreement is shown between the fitted values and the measured values. In addition, the refined discrepancy factors (R_{wp} , R_p , and χ^2), cell volume and lattice parameters of all specimens were listed in Table 1. The R_{wp} , R_p , and χ^2 values were obtained in the range of 9.6-11.1%, 6.6-8.6%, and 1.70-2.23, respectively, indicating all the refinement results are acceptable and accurate.

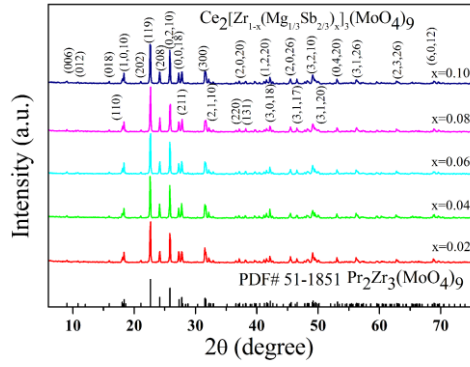


Fig. 1

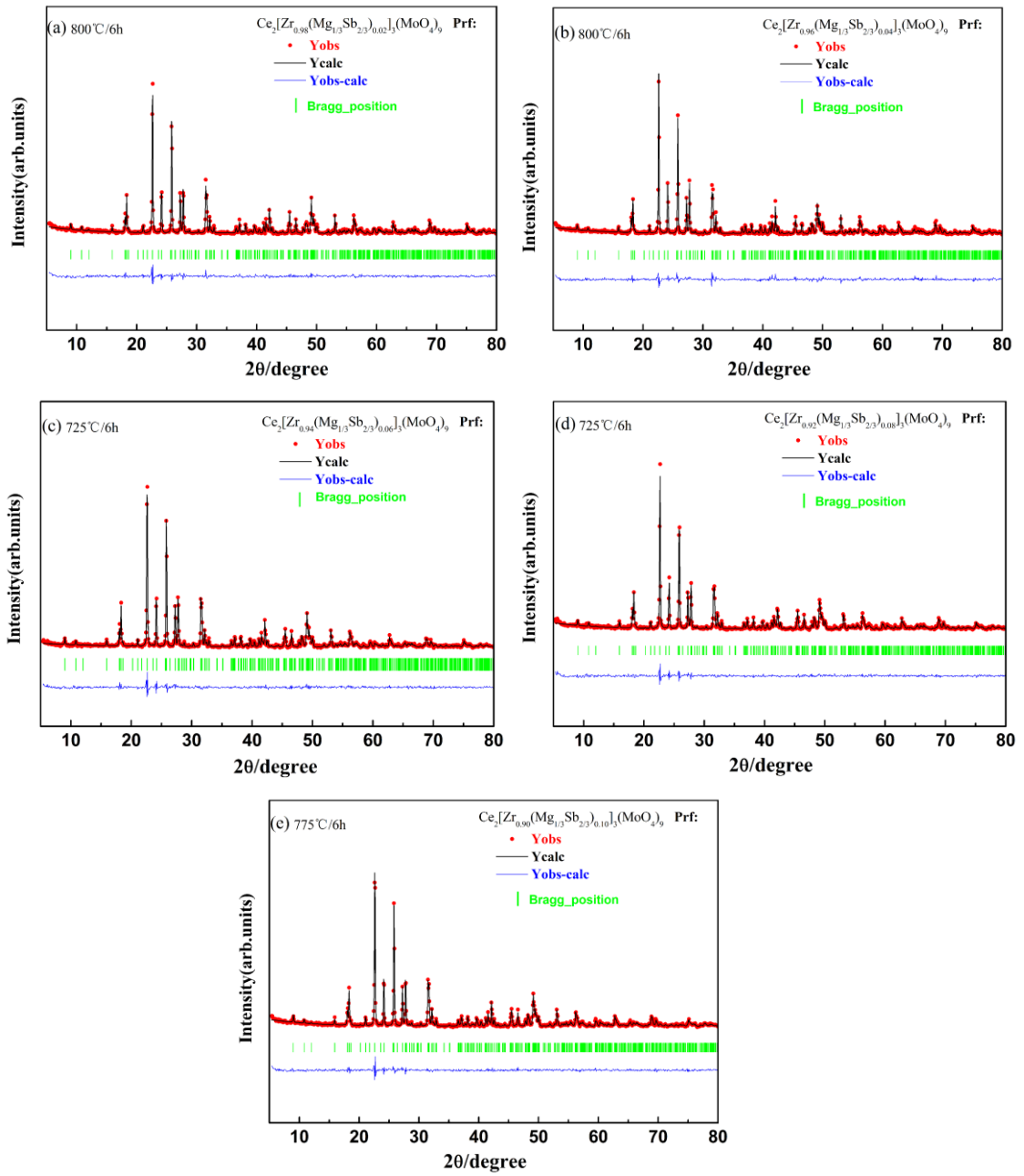


Fig. 2

With the amount of $(\text{Mg}_{1/3}\text{Sb}_{2/3})^{4+}$ increasing, the linear variation in lattice parameters (a, b and c) and unit cell volume (V_m) were presented in Fig. 3. The lattice parameter c was linearly increased while a, b and V_m linearly decreased correspondingly along with the augment of $(\text{Mg}_{1/3}\text{Sb}_{2/3})^{4+}$ because the ionic radius of Zr^{4+} (0.72 Å) is bigger than that of $(\text{Mg}_{1/3}\text{Sb}_{2/3})^{4+}$ (0.64 Å) [24,25]. The schematic illustration (in Fig. 4) and the refined atomic positions (in Table 2) of $\text{Ce}_2[\text{Zr}_{1-x}(\text{Mg}_{1/3}\text{Sb}_{2/3})_x]_3(\text{MoO}_4)_9$ samples were exhibited clearly. The crystal structure of ceramics is composed of CeO_9 , Zr/Mg/SbO_6 and MoO_4 polyhedra with common vertex angle.

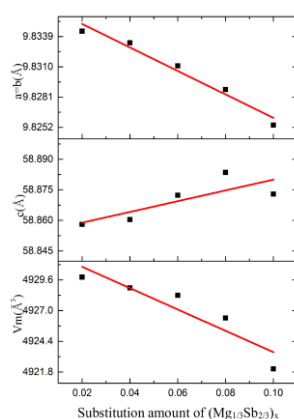


Fig. 3

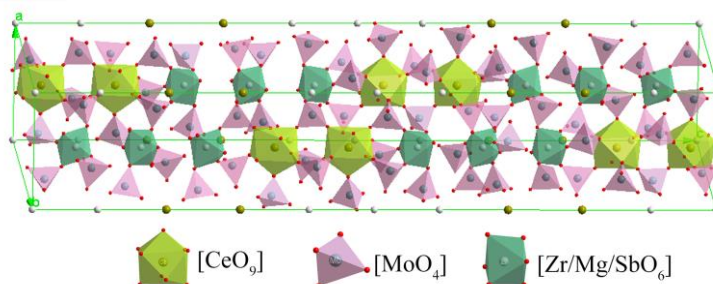


Fig. 4

The apparent densities of the $\text{Ce}_2[\text{Zr}_{1-x}(\text{Mg}_{1/3}\text{Sb}_{2/3})_x]_3(\text{MoO}_4)_9$ ($0.02 \leq x \leq 0.10$) ceramics as a function of sintering temperature were illustrated in Fig. 5. As the temperature increases, the apparent densities of each composition increases at first and then decreased slightly. For example, the apparent density of $\text{Ce}_2[\text{Zr}_{0.94}(\text{Mg}_{1/3}\text{Sb}_{2/3})_{0.06}]_3(\text{MoO}_4)_9$ ceramics increases from 3.71g/cm^3 to 3.83g/cm^3 , then the apparent density drops to 3.81g/cm^3 at 800°C . In general, an appropriate sintering temperature plays a vital role in the densification of the sample. Higher sintering temperature will accelerate the growth of crystal grains, and the pores will not be discharged in time, resulting in a non densification sample. Relative density of each composition at a high relative density was embedded in Fig. 5. The apparent densities of the major

sample was an approximate value of 3.80 g/cm^3 and relative density also has reached more than 95%. It is noticeable that the good degree of densification was in accord with the SEM results. Fig. 6(a-e) depicts the SEM microphotographs of the specimens at their optimal temperatures. It is quite clear that the dense micro-structure and unambiguous grain boundary of the specimens can be observed. As provided in Fig. 6(f), EDS of $\text{Ce}_2[\text{Zr}_{0.94}(\text{Mg}_{1/3}\text{Sb}_{2/3})_{0.06}]_3(\text{MoO}_4)_9$ ceramics was gained at 725°C for 6 h. Atom ratio of O, Mo, Zr, Ce, Sb and Mg were 73.56%, 16.91%, 5.93%, 3.48%, 0.07% and 0.05 %, respectively, which is in consistent with chemical formula.

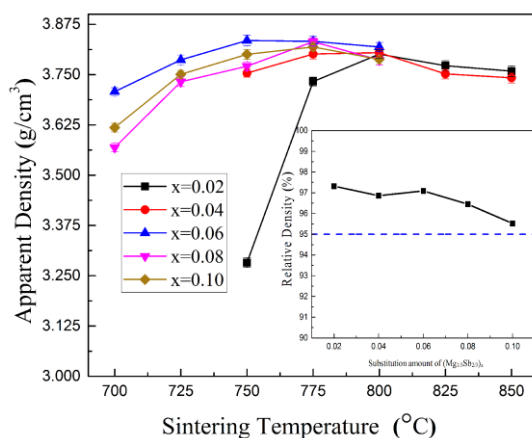


Fig. 5

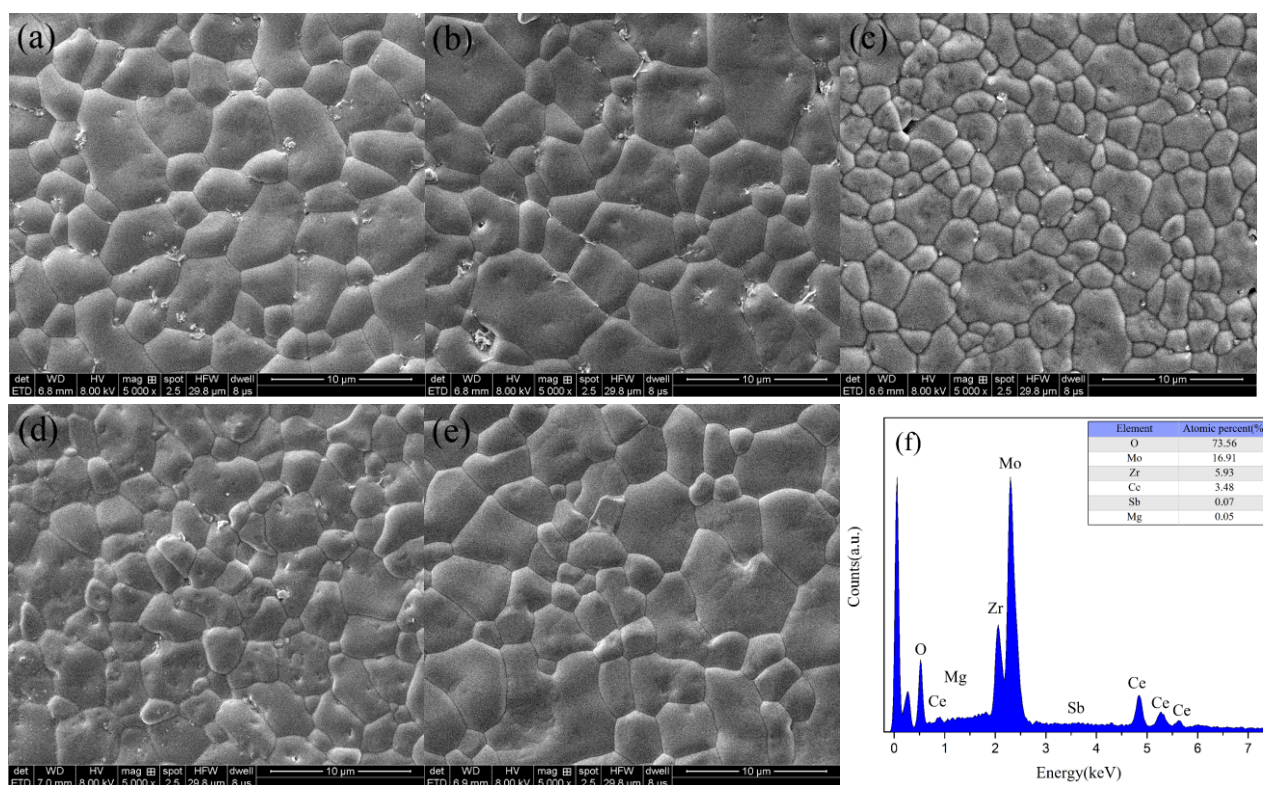


Fig. 6

The ϵ_r of ceramics with different $(\text{Mg}_{1/3}\text{Sb}_{2/3})^{4+}$ contents ($x = 0.02, 0.04, 0.06, 0.08, 0.1$) as a function of sintering temperature were revealed in Fig. 7(a). The factors that affect the ϵ_r are mainly divided into external parameters and intrinsic factors. Intrinsic factors include lattice structure and ionic polarizabilities, while external parameters include impurities, density, and second phase [26]. No secondary phase was detected in Fig. 1 and the lattice structure had no change. Thus, the dielectric constant of $\text{Ce}_2[\text{Zr}_{1-x}(\text{Mg}_{1/3}\text{Sb}_{2/3})_x]_3(\text{MoO}_4)_9$ ($0.02 \leq x \leq 0.10$) ceramics was determined mainly by apparent density. Fig. 5 shown that the apparent densities of sample increased and then decreased slightly as the temperature increases. It was easy to notice that the ϵ_r existed almost similar trend with apparent density, which indicated that the main contribution of the dielectric constant was apparent density.

The $Q \times f$ of $\text{Ce}_2[\text{Zr}_{1-x}(\text{Mg}_{1/3}\text{Sb}_{2/3})_x]_3(\text{MoO}_4)_9$ ($0.02 \leq x \leq 0.10$) ceramics sintered at 700°C - 850°C for 6 h was plotted in Fig. 7(b). The quality factor depends on the presence of intrinsic and extrinsic dielectric losses in microwave frequency. The extrinsic loss is dominated by porosity, secondary phase and lattice defects, while the intrinsic loss is mainly contributed by lattice vibrational modes [27]. It was obvious that the $Q \times f$ of each composition existed similar trend, which increased firstly and then decreased. The optimal points of $Q \times f$ were presented at 800°C , 800°C , 725°C , 725°C , 725°C and 775°C , respectively. In this study, the excellent properties of $\text{Ce}_2[\text{Zr}_{0.94}(\text{Mg}_{1/3}\text{Sb}_{2/3})_{0.06}]_3(\text{MoO}_4)_9$ ceramics ($\epsilon_r = 10.37$, $Q \times f = 71748$ GHz and $\tau_f = -13.6$ ppm/ $^\circ\text{C}$) were obtained at 725°C for 6 hours. At optimal sintering temperature, the quality factor of $\text{Ce}_2[\text{Zr}_{0.94}(\text{Mg}_{1/3}\text{Sb}_{2/3})_{0.06}]_3(\text{MoO}_4)_9$ ceramics has been greatly improved compared to previous reports, owing to the partial replacement of Zr^{4+} by $(\text{Mg}_{1/3}\text{Sb}_{2/3})^{4+}$ ions.

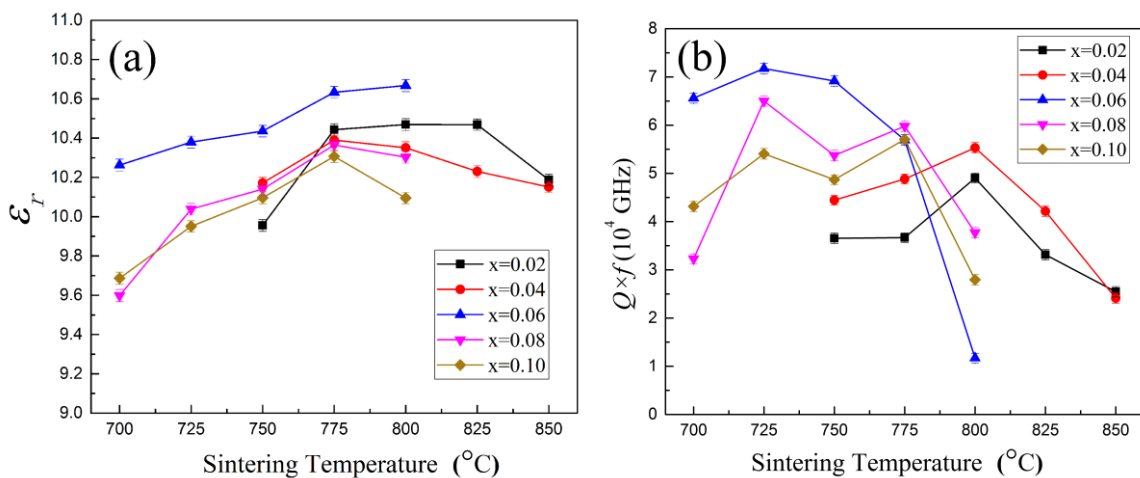
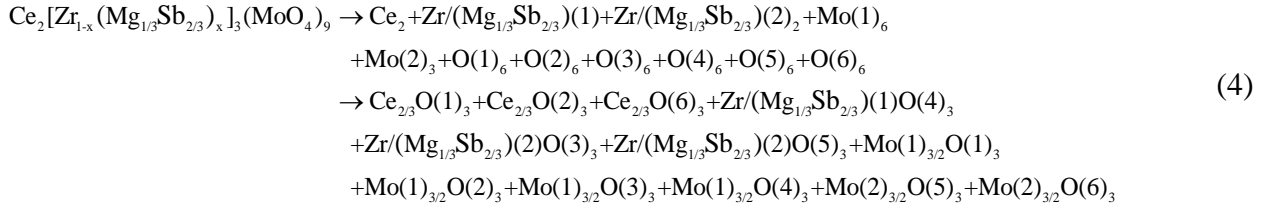


Fig. 7

As we know, chemical bonds theory of complex crystals used to characterize the intrinsic connection between chemical bond and crystal structure. Zhang [23] successfully generalized Phillips-Van Vechten-Levine (PVL) suggest that the crystalline structure parameters could be calculated by chemical bond. Any complex crystal can be decomposed into a bond equation composed of binary crystals. The bond equation of $Ce_2[Zr_{1-x}(Mg_{1/3}Sb_{2/3})_x]_3(MoO_4)_9$ ($0.02 \leq x \leq 0.10$) ceramics was shown in formula (4). In this work, there are three types of bonds which were Ce-O, Zr(Mg/Sb)-O, and Mo-O, respectively. The effective valence of cations were $N_{Ce}=3$, $N_{Zr(Mg/Sb)}=4$ and $N_{Mo}=6$, while the valence of the oxygen ion follows formula 4, and the effective valences in the Ce-O band, Zr(Mg/Sb)-O band, and Mo-O band are $-2/3$, $-4/3$, and -3 , respectively.



The bond ionicity f_i could usually be evaluated by using Eq. (5)-(9) [23,28,29]:

$$\varepsilon = \frac{n^2 - 1}{1 - f_i} + 1 \tag{5}$$

$$f_i^\mu = \frac{(C^\mu)^2}{(E_g^\mu)^2} \tag{6}$$

$$(E_g^\mu)^2 = (E_h^\mu)^2 + (C^\mu)^2 \tag{7}$$

$$(E_h^\mu)^2 = \frac{39.74}{(d^\mu)^{2.48}} \tag{8}$$

$$C^\mu = 14.4b^\mu \exp(-k_s^\mu r_0^\mu) [(Z_A^\mu)^* - \frac{n}{m}(Z_B^\mu)^*] / r_0^\mu \tag{9}$$

where E_g^μ represent the average energy gap, E_h^μ represent the homopolar part, C^μ represent the heteropolar part and $\exp(-k_s^\mu r_0^\mu)$ is Thomas-Fermi screening factor [30].

The bond ionicity f_i were explored quantitatively as shown in Table 3. In addition, ε_r and an individual bond ionicity $f_{i(Mo1-O(2))}$ as a function of the content of $(Mg_{1/3}Sb_{2/3})^{4+}$ substitution were shown in Fig. 8. The ε_r values display a decreasing tendency from 10.47 to 10.03 along with the augment of $(Mg_{1/3}Sb_{2/3})^{4+}$. The positive correlation between relative permittivity and f_i was described in formula (5).

As increasing of $(\text{Mg}_{1/3}\text{Sb}_{2/3})^{4+}$ contents, $f_{i(\text{Mo1-O}(2))}$ and ϵ_r values show the same tendency which indicated the ϵ_r values were strongly dependent on $f_{i(\text{Mo1-O}(2))}$.

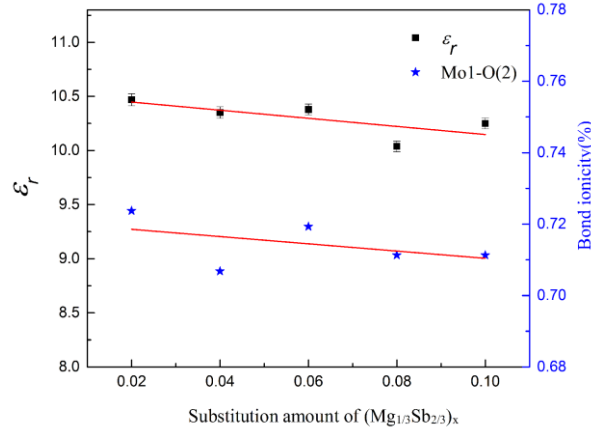


Fig. 8

Lattice energy can be used to predict and explain many physical and chemical properties of ionic crystals, so larger lattice energy, the more stable structure. The lattice energy U (in Table 4) of specimen could be evaluated according to the following formulas (10)-(13) [23,28,29]. Fig. 9 presented $U_{(\text{Zr}(\text{Mg}/\text{Sb})1-\text{O}(4))}$ values and the quality factor $Q \times f$ as a variation of $(\text{Mg}_{1/3}\text{Sb}_{2/3})^{4+}$ substitution. The $Q \times f$ values were increased from 49033 GHz to 64012 GHz, and then decreased to 48690 GHz. They all show the same trend of increasing first and then decreasing, indicating that $Q \times f$ is mainly affected by $U_{(\text{Zr}(\text{Mg}/\text{Sb})1-\text{O}(4))}$.

$$U_{\text{cal}} = \sum_{\mu} U_b^{\mu} \quad (10)$$

$$U_b^{\mu} = U_{bc}^{\mu} + U_{bi}^{\mu} \quad (11)$$

$$U_{bc}^{\mu} = 2100m \frac{(Z_A^{\mu})^{1.64}}{(d^{\mu})^{0.75}} f_C^{\mu} \quad (12)$$

$$U_{bi}^{\mu} = 1270 \frac{(m+n)Z_A^{\mu}Z_B^{\mu}}{d^{\mu}} \left(1 - \frac{0.4}{d^{\mu}}\right) f_i^{\mu} \quad (13)$$

Where U_{bi}^{μ} and U_{bc}^{μ} represent ionic energy part and covalent energy part.

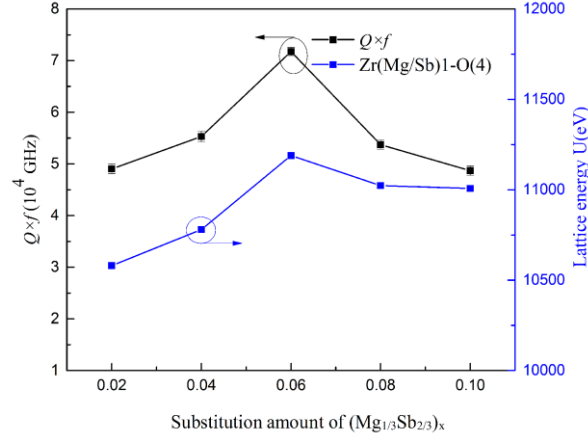


Fig. 9

Zhang [31,32] had reported a strong relationship between bond energy E and τ_f , which the larger bond energy, the closer to zero the τ_f value. The E value of an individual bond μ could be calculated by Eq. (14)-(18) [33-35]:

$$E^\mu = t_c E_c^\mu + t_i E_i^\mu \quad (14)$$

$$E_c^\mu = \frac{(r_{cA} + r_{cB})}{d^\mu} (E_{A-A} E_{B-B})^{1/2} (KJ / mol) \quad (15)$$

$$E_i^\mu = \frac{1389.088}{d^\mu} (KJ / mol) \quad (16)$$

$$t_i = \left| \frac{(S_A - S_B)}{6} \right| \quad (17)$$

$$t_c + t_i = 1 \quad (18)$$

where S represent the electronegativity of ions; t_i and t_c are covalent and ionic blending coefficient; r_c is covalent radii; E_{A-A} and E_{B-B} are homonuclear bond energy [36].

The τ_f and an individual bond ionicity $E_{(Mo1-O(1))}$ as a function of the content of $(Mg_{1/3}Sb_{2/3})^{4+}$ substitution were illustrated in Fig. 10. In addition, the calculated bond energy E are shown in Table 5. The τ_f values of ceramics fluctuated slightly between -8.59 ppm/ $^{\circ}C$ and -13.69 ppm/ $^{\circ}C$ with $(Mg_{1/3}Sb_{2/3})^{4+}$ increasing in our experiments. The bond energy $E_{(Mo1-O(1))}$ and τ_f have the same trend, indicating that τ_f is mainly influenced by $E_{(Mo1-O(1))}$.

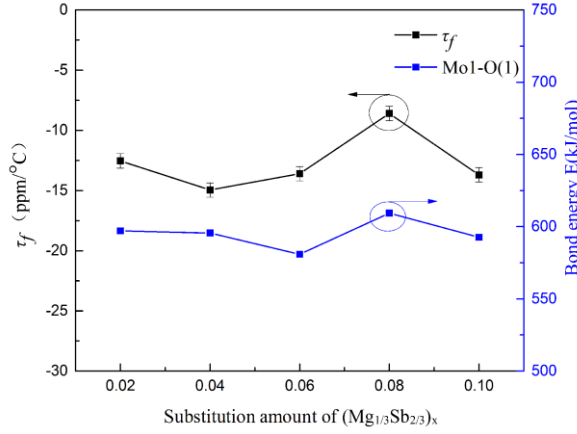


Fig. 10

The τ_f is obtained by Eq. (19) and the α is described via Eq. (20)-(23):

$$\tau_f = -\left(\frac{\tau_\varepsilon}{2} + \alpha\right) \quad (19)$$

$$\alpha = \sum_{\mu} F_{mn}^{\mu} \alpha_{mn}^{\mu} \quad (20)$$

$$\alpha_{mn}^{\mu} = -3.1685 + 0.8376\gamma_{mn} \quad (21)$$

$$\gamma_{mn} = \frac{kZ_A^{\mu} N_{CA}^{\mu}}{U_b^{\mu} \Delta_A} \beta_{mn} \quad (22)$$

$$\beta_{mn} = \frac{m(m+n)}{2n} \quad (23)$$

Where Z_A^{μ} represent the valence states of cation, k is Boltzmann constant, N_{CA}^{μ} represent the coordination number of cation, τ_ε is temperature coefficient of the dielectric constant, F_{mn}^{μ} represent the proportion of μ bond. Calculated α values were shown in Table 6. Obviously, the value of $\alpha_{Zr(Mg/Sb)-O}$ and α_{Ce-O} were positive. The value of α_{Mo-O} had a positive influence on τ_f because of $\alpha_{Mo-O} < 0$.

As is known, it is difficult to detect the intrinsic loss and extrinsic loss of microwave dielectric ceramics by conventional testing methods. Far-infrared spectral analysis can reflect the intrinsic loss to a certain extent. These spectra were analyzed by using the classical harmonic oscillator model was applied to study infrared spectroscopy. It relies on two formulas: the standard Lorentzian formula (Eq. (24)) and the Fresnel formula (Eq. (25)) [37,38]. The dielectric loss tangent $\tan\delta$ is evaluated by Eq. (26).

$$\varepsilon^*(\omega) = \varepsilon_\infty + \sum_{j=1}^n \frac{\omega_{pj}^2}{\omega_{oj}^2 - \omega^2 + j\omega\gamma_j} \quad (24)$$

$$R = \left| \frac{1 - \sqrt{\varepsilon^*(\omega)}}{1 + \sqrt{\varepsilon^*(\omega)}} \right|^2 \quad (25)$$

$$\tan \delta = \frac{\varepsilon''}{\varepsilon'} = \frac{\sum_{j=1}^n \Delta \varepsilon_j (\gamma_j \omega) / \omega_{oj}^2}{\varepsilon_\infty + \sum_{j=1}^n \Delta \varepsilon_j} \quad (26)$$

where γ_j is damping factor; ε_∞ is dielectric constant; ω_{pj} is plasma frequency; $\varepsilon^*(\omega)$ is a complex dielectric function; ω_{oj} is the eigen frequency; n is the number of transverse phonon modes. ω_{pj} is plasma frequency; R is the IR reflectivity.

As shown in Fig. 11(a), the fitted infrared spectra of the $\text{Ce}_2[\text{Zr}_{0.94}(\text{Mg}_{1/3}\text{Sb}_{2/3})_{0.06}]_3(\text{MoO}_4)_9$ sample is depicted. The fitted infrared reflectivity spectrum were in good agreement with measured part. In addition, real and imaginary parts of the permittivity were given in Fig. 11(b). Table 7 lists the fitted phonon parameters, indicating it was fitted with sixteen modes. As compared with the measured permittivity, the calculated one was slightly big. The measured value (1.35×10^{-4}) and calculated value (2.68×10^{-4}) of the dielectric loss remained in the same order of magnitude. Both the fitted and measured values correspond well, which indicated that in the microwave frequencies, the dielectric polarization mainly caused by absorption of phonons in the infrared region [39,40].

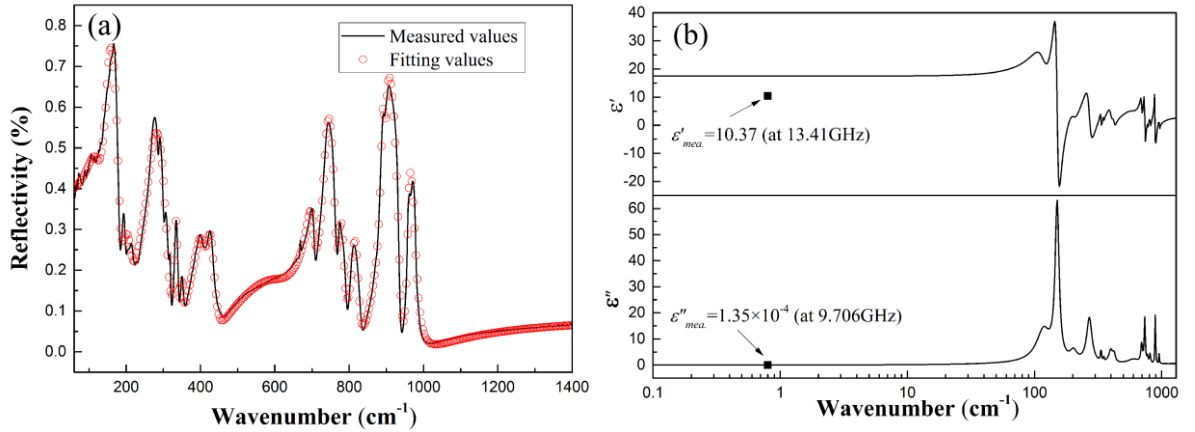


Fig. 11

4. Conclusion

$\text{Ce}_2[\text{Zr}_{1-x}(\text{Mg}_{1/3}\text{Sb}_{2/3})_x]_3(\text{MoO}_4)_9$ ($x=0.02, 0.04, 0.06, 0.08$ and 0.10) ceramics were fabricated well via the traditional solid-state method. The pure-phase with space group of R-3c was detected for all specimens. The dense micro-structure and clear grain boundary of the specimens can be observed in SEM

photos. The crystal structure was investigated deeply by the Rietveld refinement method. The ε_r , $Q \times f$ and τ_f values of these samples were strongly dependent on chemical bonds such as $f_{i(\text{Mo1-O}(2))}$, $U_{(\text{Zr}(\text{Mg/Sb})1\text{-O}(4))}$ and $E_{(\text{Mo1-O}(1))}$, respectively. The infrared reflectivity spectrum were in good agreement with the dielectric properties of samples. Meanwhile, $\text{Ce}_2[\text{Zr}_{0.94}(\text{Mg}_{1/3}\text{Sb}_{2/3})_{0.06}]_3(\text{MoO}_4)_9$ ceramic with $\varepsilon_r = 10.37$, $Q \times f = 71748$ GHz and $\tau_f = -13.6$ ppm/ $^\circ\text{C}$, were obtained at 725°C for 6 hours.

Acknowledgments

This work was supported by the National Natural Science Foundation (No. 51972143). The authors would like to thank the administrators in IR beamline workstation of National Synchrotron Radiation Laboratory (NSRL) for the help in IR measurement.

References

- [1] Guo HH, Zhou D, Liu WF, *et al.* Microwave dielectric properties of temperature-stable zircon-type (Bi, Ce)VO₄ solid solution ceramics. *J Am Ceram Soc* 2020, **103**: 423-431.
- [2] Xiang HC, Fang L, Fang WS, *et al.* A novel low-firing microwave dielectric ceramic Li₂ZnGe₃O₈ with cubic spinel structure. *J Eur Ceram Soc* 2017, **37**: 625-629.
- [3] Manan A, Ullah Z, Ahmad AS, *et al.* Phase microstructure evaluation and microwave dielectric properties of (1-x)Mg_{0.95}Ni_{0.05}Ti_{0.98}Zr_{0.02}O_{3-x}Ca_{0.6}La_{0.8/3}TiO₃ ceramics. *J Adv Ceram* 2018, **7**: 72-78.
- [4] Zheng JJ, Yang YK, Wu HT, *et al.* Structure, infrared spectra and microwave dielectric properties of the novel Eu₂TiO₅ ceramics. *J Am Ceram Soc* 2020, **103**: 4333-4341.
- [5] Li CC, Xiang HC, Xu MY, *et al.* Li₂AGeO₄ (A = Zn, Mg): Two novel low-permittivity microwave dielectric ceramics with olivine structure. *J Eur Ceram Soc* 2018, **38**: 1524-1528.
- [6] Chen XL, Li X, Zhou HF, *et al.* Phase evolution, microstructure, electric properties of (Ba_{1-x}Bi_{0.67x}Na_{0.33x})(Ti_{1-x}Bi_{0.33x}Sn_{0.67x})O₃ ceramics. *J Adv Ceram* 2019, **8**: 427-437.
- [7] Li J, Fang L, Luo H, *et al.* Li₄WO₅: A temperature stable low-firing microwave dielectric ceramic with rock salt structure. *J Eur Ceram Soc* 2016, **36**: 243-246.
- [8] Zhang YH, Wu HT. Crystal structure and microwave dielectric properties of La₂(Zr_{1-x}Ti_x)₃(MoO₄)₉ (0 ≤ x ≤ 0.1) ceramics. *J Am Ceram Soc* 2019, **102**: 4092-4102.
- [9] Bi JX, Xing CF, Yang CH, *et al.* Phase composition, microstructure and microwave dielectric properties of rock salt structured Li₂ZrO₃-MgO ceramics. *J Eur Ceram Soc* 2018, **38**: 3840-3846.
- [10] Fang L, Wei ZH, Su CX, *et al.* Novel low-firing microwave dielectric ceramics: BaMV₂O₇ (M = Mg, Zn). *Ceram Int* 2014, **40**: 16835-16839.
- [11] Pang LX, Zhou D. Modification of NdNbO₄ microwave dielectric ceramic by Bi substitutions. *J Am Ceram Soc* 2019, **102**: 2278-2282.
- [12] Wu MJ, Zhang YC, Xiang MQ. Synthesis, characterization and dielectric properties of a novel temperature stable (1-x)CoTiNb₂O_{8-x}ZnNb₂O₆ ceramic. *J Adv Ceram* 2019, **8**: 228-237.
- [13] Zhou D, Pang LX, Wang DW, *et al.* High permittivity and low loss microwave dielectrics suitable for 5G resonators and low temperature co-fired ceramic architecture. *J Mater Chem C* 2017, **5**: 10094-10098.

- [14] Qin TY, Zhong CW, Qin Y, *et al.* Low-temperature sintering mechanism and microwave dielectric properties of ZnAl₂O₄-LMZBS composites. *J Alloy Compd* 2019, **797**: 744-753.
- [15] Huang FY, Su H, Li YX, *et al.* Low-temperature sintering and microwave dielectric properties of CaMg_{1-x}Li_{2x}Si₂O₆ (x = 0-0.3) ceramics. *J Adv Ceram* 2020, **9**: 471-480.
- [16] Xiang HC, Li CC, Jantunen H, *et al.* Ultralow loss CaMgGeO₄ microwave dielectric ceramic and its chemical compatibility with silver electrodes for low-temperature cofired ceramic applications. *ACS Sustain Chem Eng* 2018, **6**: 6458-6466.
- [17] Guo HH, Zhou D, Pang LX, *et al.* Microwave dielectric properties of low firing temperature stable scheelite structured (Ca, Bi)(Mo, V)O₄ solid solution ceramics for LTCC applications. *J Eur Ceram Soc* 2019, **39**: 2365-2373.
- [18] Hsiang HI, Chen CC, Yang SY. Microwave dielectric properties of Ca_{0.7}Nd_{0.2}TiO₃ ceramic-filled CaO-B₂O₃-SiO₂ glass for LTCC applications. *J Adv Ceram* 2019, **8**: 345-351.
- [19] Liu W, Zuo R. Low temperature fired Ln₂Zr₃(MoO₄)₉ (Ln=Sm, Nd) microwave dielectric ceramics. *Ceram Int* 2017, **43**: 17229-17232.
- [20] Zhang YH, Sun JJ, Dai N, *et al.* Crystal structure, infrared spectra and microwave dielectric properties of novel extra low-temperature fired Eu₂Zr₃(MoO₄)₉ ceramics. *J Eur Ceram Soc* 2019, **39**: 1127-1131.
- [21] Tao BJ, Xing CF, Wang WF, *et al.* A novel Ce₂Zr₃(MoO₄)₉ microwave dielectric ceramic with ultra-low firing temperature. *Ceram Int* 2019, **45**: 24675-24683.
- [22] Xiao M, He SS, Meng J, *et al.* Bond ionicity, lattice energy, bond energy and the microwave dielectric properties of non-stoichiometric MgZrNb_{2+x}O_{8+2.5x} ceramics. *Mater Chem Phys* 2020, **242**: 122412.
- [23] Wu ZJ, Meng QB, Zhang SY. Semiempirical study on the valences of Cu and bond covalency in Y_{1-x}Ca_xBa₂Cu₃O_{6-y}. *Phys Rev B* 1998, **58**: 958-962.
- [24] Kim SH, Kim ES. Intrinsic factors affecting the microwave dielectric properties of Mg₂Ti_{1-x}(Mg_{1/3}Sb_{2/3})_xO₄ ceramics. *Ceram Int* 2016, **42**: 15035-15040.
- [25] Pei CJ, Tan JJ, Li Y, *et al.* Effect of Sb-site nonstoichiometry on the structure and microwave dielectric properties of Li₃Mg₂Sb_{1-x}O₆ ceramics. *J Adv Ceram* 2020, **9**: 588-594.

- [26] Xia WS, Zhang LY, Wang Y, *et al.* Extrinsic effects on microwave dielectric properties of high-Q MgZrTa₂O₈ ceramics. *J Mater Sci:Mater Electron* 2016, **27**: 11325-11330.
- [27] Silverman BD. Microwave Absorption in Cubic Strontium Titanate. *Phys Rev* 1962, **125**: 1921-1930.
- [28] Xue DF, Zhang SY. Calculation of the nonlinear optical coefficient of the NdAl₃(BO₃)₄ crystal. *J Phys Condens Matter* 1996, **8**: 1949-1956.
- [29] Berkov DV. Evaluation of the energy barrier distribution in many-particle systems using the path integral approach. *J Phys Condens Matter* 1998, **10**: L89-L95.
- [30] Levine BF. Bond susceptibilities and ionicities in complex crystal structures. *J Chem Phys* 1973, **59**: 1463-1486.
- [31] Zhang P, Zhao YG, Wang XY. The correlations between electronic polarizability, packing fraction, bond energy and microwave dielectric properties of Nd(Nb_{1-x}Sb_x)O₄ ceramics. *J Alloy Compd* 2015, **644**: 621-625.
- [32] Zhang P, Zhao YG. Effects of structural characteristics on microwave dielectric properties of Li₂Mg(Ti_{1-x}Mn_x)₃O₈ ceramics. *J Alloy Compd* 2015, **647**: 386-391.
- [33] Sanderson RT. Multiple and single bond energies in inorganic molecules. *J Inorg Nucl Chem* 1968, **30**: 375-393.
- [34] Sanderson RT. Chemical bonds, bond energy. New York(US): Academic press, 1971.
- [35] Sanderson RT. Electronegativity and bond energy. *J Am Ceram Soc* 1983, **105**: 2259-2261.
- [36] Luo YR. Comprehensive handbook of chemical bond energies. Boca Raton(US): CRC press, 2007.
- [37] Chen Z, Jia H, Sharafudeen K, *et al.* Up-conversion luminescence from single vanadate through blackbody radiation harvesting broadband near-infrared photons for photovoltaic cells. *J Alloy Compd* 2016, **663**: 204-210.
- [38] Guo J, Zhou D, Wang L, *et al.* Infrared spectra, Raman spectra, microwave dielectric properties and simulation for effective permittivity of temperature stable ceramics AMoO₄-TiO₂ (A=Ca, Sr). *Dalton Trans* 2013, **42**: 1483-1491.
- [39] Pang LX, Zhou D, Qi ZM, *et al.* Structure-property relationships of low sintering temperature scheelite-structured (1-x)BiVO₄-xLaNbO₄ microwave dielectric ceramics. *J Mater Chem C* 2017, **5**: 2695-2701.

[40] Li JM, Zhang CM, Liu H, *et al.* Structure, morphology, and microwave dielectric properties of SmAlO₃ synthesized by stearic acid route. *J Adv Ceram* 2020, **9**: 558-566.

Figure captions

Fig. 1. XRD patterns of $\text{Ce}_2[\text{Zr}_{1-x}(\text{Mg}_{1/3}\text{Sb}_{2/3})_x]_3(\text{MoO}_4)_9$ ($x = 0.02, 0.04, 0.06, 0.08$ and 0.1) ceramics sintered at densification temperature for 6 h

Fig. 2. Refinement results of $\text{Ce}_2[\text{Zr}_{1-x}(\text{Mg}_{1/3}\text{Sb}_{2/3})_x]_3(\text{MoO}_4)_9$ ceramics calcined under various conditions as indicated: (a) $x = 0.02$, (b) $x = 0.04$, (c) $x = 0.06$, (d) $x = 0.08$, (e) $x = 0.10$

Fig. 3. The lattice parameters (a , b and c) and unit cell volume (V_m) of $\text{Ce}_2[\text{Zr}_{1-x}(\text{Mg}_{1/3}\text{Sb}_{2/3})_x]_3(\text{MoO}_4)_9$ ceramics as a function of the substitution amount of $(\text{Mg}_{1/3}\text{Sb}_{2/3})^{4+}$.

Fig. 4. The schematic illustration of $\text{Ce}_2[\text{Zr}_{1-x}(\text{Mg}_{1/3}\text{Sb}_{2/3})_x]_3(\text{MoO}_4)_9$ ceramics

Fig. 5. Apparent densities of the $\text{Ce}_2[\text{Zr}_{1-x}(\text{Mg}_{1/3}\text{Sb}_{2/3})_x]_3(\text{MoO}_4)_9$ ceramics as a function of the sintering temperature.

Fig. 6. SEM microphotographs of $\text{Ce}_2[\text{Zr}_{1-x}(\text{Mg}_{1/3}\text{Sb}_{2/3})_x]_3(\text{MoO}_4)_9$ ceramics at densification temperature for 6 h: (a) $x = 0.02$, (b) $x = 0.04$, (c) $x = 0.06$, (d) $x = 0.08$, (e) $x = 0.10$; (f) EDS analysis of $\text{Ce}_2[\text{Zr}_{0.94}(\text{Mg}_{1/3}\text{Sb}_{2/3})_{0.06}]_3(\text{MoO}_4)_9$ ceramics sintered at 725°C for 6 h.

Fig. 7. $Q \times f$, and ϵ_r values of $\text{Ce}_2[\text{Zr}_{1-x}(\text{Mg}_{1/3}\text{Sb}_{2/3})_x]_3(\text{MoO}_4)_9$ ceramics sintered at $700\text{--}800^\circ\text{C}$: (a) ϵ_r , (b) $Q \times f$

Fig. 8. ϵ_r and the Mo1-O(2) bond ionicity of $\text{Ce}_2[\text{Zr}_{1-x}(\text{Mg}_{1/3}\text{Sb}_{2/3})_x]_3(\text{MoO}_4)_9$ ceramics as a function of the content of $(\text{Mg}_{1/3}\text{Sb}_{2/3})^{4+}$ substitution

Fig. 9. $Q \times f$ and the Zr(Mg/Sb)1-O(4) lattice energy of $\text{Ce}_2[\text{Zr}_{1-x}(\text{Mg}_{1/3}\text{Sb}_{2/3})_x]_3(\text{MoO}_4)_9$ ceramics as a function of the content of $(\text{Mg}_{1/3}\text{Sb}_{2/3})^{4+}$ substitution

Fig. 10. τ_f and the Mo1-O(1) bond energy of $\text{Ce}_2[\text{Zr}_{1-x}(\text{Mg}_{1/3}\text{Sb}_{2/3})_x]_3(\text{MoO}_4)_9$ ceramics as a function of the content of $(\text{Mg}_{1/3}\text{Sb}_{2/3})^{4+}$ substitution

Fig. 11(a). Measured (black line) and fitted (red line) infrared reflectivity spectrum, and (b) real and imaginary parts of the complex permittivity for $\text{Ce}_2[\text{Zr}_{0.94}(\text{Mg}_{1/3}\text{Sb}_{2/3})_{0.06}]_3(\text{MoO}_4)_9$ ceramic sintered at 725°C for 6 h

Table 1 The refinement parameters of $\text{Ce}_2[\text{Zr}_{1-x}(\text{Mg}_{1/3}\text{Sb}_{2/3})_x]_3(\text{MoO}_4)_9$ ceramics sintered at optimized sintering temperature.

Table 2 The refined atomic positions of $\text{Ce}_2[\text{Zr}_{1-x}(\text{Mg}_{1/3}\text{Sb}_{2/3})_x]_3(\text{MoO}_4)_9$ samples.

Table 3 The bond ionicity f_i of $\text{Ce}_2[\text{Zr}_{1-x}(\text{Mg}_{1/3}\text{Sb}_{2/3})_x]_3(\text{MoO}_4)_9$ ($x=0.02-0.10$) ceramics sintered at densification temperature for 6 h.

Table 4 The lattice energy U of $\text{Ce}_2[\text{Zr}_{1-x}(\text{Mg}_{1/3}\text{Sb}_{2/3})_x]_3(\text{MoO}_4)_9$ ($x=0.02-0.10$) ceramics sintered at densification temperature for 6 h.

Table 5 The bond energy E of $\text{Ce}_2[\text{Zr}_{1-x}(\text{Mg}_{1/3}\text{Sb}_{2/3})_x]_3(\text{MoO}_4)_9$ ($x=0.02-0.10$) ceramics sintered at densification temperature for 6 h.

Table 6 The coefficient of thermal expansion α of $\text{Ce}_2[\text{Zr}_{1-x}(\text{Mg}_{1/3}\text{Sb}_{2/3})_x]_3(\text{MoO}_4)_9$ ($x=0.02-0.10$) ceramics sintered at densification temperature for 6 h.

Table 7 The phonon parameters after fitting of the $\text{Ce}_2[\text{Zr}_{0.94}(\text{Mg}_{1/3}\text{Sb}_{2/3})_{0.06}]_3(\text{MoO}_4)_9$ sample sintered at 725 °C for 6 h.

Table 1

Structural parameters	Ce ₂ [Zr _{1-x} (Mg _{1/3} Sb _{2/3}) _x] ₃ (MoO ₄) ₉				
	X=0.02	X=0.04	X=0.06	X=0.08	X=0.10
$a=b$ (Å)	9.8344	9.8333	9.8310	9.8288	9.8254
c (Å)	58.8580	58.8603	58.8723	58.8835	58.8729
$\alpha=\beta$ (°)	90	90	90	90	90
γ (°)	120	120	120	120	120
V_m (Å ³)	4929.84	4928.92	4928.30	4926.38	4922.07
R_p (%)	8.33	8.52	6.60	7.62	7.46
R_{wp} (%)	10.60	11.10	10.50	9.60	9.51
χ^2	2.04	2.23	1.90	1.70	1.71

Table 2

Atom	Wyckoff position	Site	x	y	z	Occupancy
Ce	12c	3	0.6667	0.3333	0.0297	0.3333
Zr1	6b	-3	0.0000	0.0000	0.0000	0.1667
Zr2	12c	3	0.3333	0.6667	0.0712	0.3333
Mo1	36f	1	0.0982	0.7275	0.0250	1.0000
Mo2	18e	2	0.2834	0.2834	0.2500	0.5000
O1	36f	1	-0.0959	0.5941	0.0308	1.0000
O2	36f	1	0.1628	0.6664	0.0027	1.0000
O3	36f	1	0.2061	0.7312	0.0500	1.0000
O4	36f	1	0.1192	0.9207	0.0201	1.0000
O5	36f	1	0.2879	0.4692	0.2456	1.0000
O6	36f	1	0.1708	0.1902	0.2729	1.0000

Table 3

Ce ₂ [Zr _{1-x} (Mg _{1/3} Sb _{2/3}) _x] ₃ (MoO ₄) ₉	Bond ionicity f_i (%)				
	x=0.02	x=0.04	x=0.06	x=0.08	x=0.1
Ce-O(1) ¹	0.8484	0.8518	0.8467	0.8488	0.8491
Ce-O(1) ²	0.8484	0.8518	0.8467	0.8489	0.8491
Ce-O(1) ³	0.8485	0.8518	0.8467	0.8489	0.8491
Ce-O(2) ¹	0.8527	0.8527	0.8553	0.8561	0.8558
Ce-O(2) ²	0.8527	0.8527	0.8553	0.8561	0.8558
Ce-O(2) ³	0.8527	0.8527	0.8553	0.8561	0.8558
Ce-O(6) ¹	0.8523	0.8540	0.8524	0.8544	0.8520
Ce-O(6) ²	0.8523	0.8540	0.8524	0.8544	0.8521
Ce-O(6) ³	0.8523	0.8540	0.8524	0.8545	0.8521
Zr(Mg/Sb)1-O(4)×6	0.7964	0.7868	0.7851	0.7873	0.7880
Zr(Mg/Sb)2-O(3) ¹	0.7912	0.7757	0.8014	0.7895	0.7978
Zr(Mg/Sb)2-O(3) ²	0.7912	0.7758	0.8015	0.7895	0.7978
Zr(Mg/Sb)2-O(3) ³	0.7913	0.7758	0.8015	0.7895	0.7979
Zr(Mg/Sb)2-O(5) ¹	0.7849	0.7824	0.7920	0.7884	0.7891
Zr(Mg/Sb)2-O(5) ²	0.7850	0.7824	0.7920	0.7884	0.7891
Zr(Mg/Sb)2-O(5) ³	0.7850	0.7825	0.7920	0.7885	0.7892
Mo1-O(1)	0.7237	0.7167	0.7298	0.7194	0.7251
Mo1-O(2)	0.7237	0.7068	0.7193	0.7113	0.7113
Mo1-O(3)	0.7315	0.7344	0.7248	0.7348	0.7237
Mo1-O(4)	0.7369	0.7269	0.7474	0.7377	0.7363
Mo2-O(5)×2	0.7248	0.7344	0.7338	0.7381	0.7288
Mo2-O(6)×2	0.7276	0.7064	0.7268	0.7183	0.7258

Table 4

Ce ₂ [Zr _{1-x} (Mg _{1/3} Sb _{2/3}) _x] ₃ (MoO ₄) ₉	Lattice energy <i>U</i> (eV)				
	x=0.02	x=0.04	x=0.06	x=0.08	x=0.1
Ce-O(1) ¹	3364	3208	3413	3352	3354
Ce-O(1) ²	3364	3207	3412	3351	3352
Ce-O(1) ³	3364	3207	3412	3351	3352
Ce-O(2) ¹	3276	3188	3235	3200	3212
Ce-O(2) ²	3276	3188	3234	3199	3212
Ce-O(2) ³	3276	3188	3234	3199	3211
Ce-O(6) ¹	3285	3160	3296	3236	3291
Ce-O(6) ²	3284	3160	3295	3235	3291
Ce-O(6) ³	3284	3159	3295	3234	3291
Zr(Mg/Sb)1-O(4)×6	10580	10780	11189	11023	11007
Zr(Mg/Sb)2-O(3) ¹	10844	11319	10360	10916	10512
Zr(Mg/Sb)2-O(3) ²	10842	11317	10358	10914	10510
Zr(Mg/Sb)2-O(3) ³	10842	11315	10358	10913	10509
Zr(Mg/Sb)2-O(5) ¹	11152	10998	10850	10968	10955
Zr(Mg/Sb)2-O(5) ²	11151	10997	10849	10967	10954
Zr(Mg/Sb)2-O(5) ³	11149	10995	10847	10965	10951
Mo1-O(1)	43980	43859	43164	44597	43763
Mo1-O(2)	43964	45433	44862	45862	45940
Mo1-O(3)	42658	40742	43989	42023	43995
Mo1-O(4)	41707	42121	39969	41489	41852
Mo2-O(5)×2	43793	40747	42479	41418	43146
Mo2-O(6)×2	43329	45493	43655	44782	43658

Table 5

Ce ₂ [Zr _{1-x} (Mg _{1/3} Sb _{2/3}) _x] ₃ (MoO ₄) ₉	Bond energy <i>E</i> (kJ/mol)				
	x=0.02	x=0.04	x=0.06	x=0.08	x=0.1
Ce-O(1) ¹	420.9821	397.1351	428.3333	419.0938	419.3161
Ce-O(1) ²	420.8959	397.0431	428.2441	418.9913	419.2306
Ce-O(1) ³	420.8097	396.9971	428.1549	418.9230	419.1622
Ce-O(2) ¹	407.8353	394.2862	401.9027	396.5835	398.4747
Ce-O(2) ²	407.7868	394.2408	401.8555	396.5376	398.4283
Ce-O(2) ³	407.7382	394.1954	401.8084	396.4917	398.3820
Ce-O(6) ¹	409.1178	390.1848	410.8842	401.8398	410.1627
Ce-O(6) ²	409.0527	390.1552	410.8513	401.7927	410.1136
Ce-O(6) ³	409.0038	390.0811	410.7692	401.7299	410.0482
Zr(Mg/Sb)1-O(4)×6	483.6989	494.9655	519.9098	509.8280	508.8463
Zr(Mg/Sb)2-O(3) ¹	499.2091	527.2509	470.9886	503.4523	479.7139
Zr(Mg/Sb)2-O(3) ²	499.0641	527.0891	470.8595	503.3048	479.5799
Zr(Mg/Sb)2-O(3) ³	499.0158	527.0352	470.8380	503.2557	479.5353
Zr(Mg/Sb)2-O(5) ¹	517.6120	507.9184	499.6205	506.5205	505.7748
Zr(Mg/Sb)2-O(5) ²	517.5340	507.8684	499.5479	506.4707	505.7003
Zr(Mg/Sb)2-O(5) ³	517.3781	507.7182	499.4268	506.3214	505.5515
Mo1-O(1)	597.0129	595.5327	580.8629	609.3766	592.6962
Mo1-O(2)	596.7025	627.2896	614.5251	635.2764	636.8040
Mo1-O(3)	571.2568	536.2299	597.0474	559.2248	597.2891
Mo1-O(4)	553.2635	561.9021	521.2639	549.2328	555.9438
Mo2-O(5)×2	593.3090	536.3134	567.7086	547.9217	580.6343
Mo2-O(6)×2	584.2142	628.5494	590.4598	613.1024	590.6287

Table 6

Ce ₂ [Zr _{1-x} (Mg _{1/3} Sb _{2/3}) _x] ₃ (MoO ₄) ₉	Thermal expansion coefficient α (10 ⁻⁶ /K)				
	x=0.02	x=0.04	x=0.06	x=0.08	x=0.1
Ce-O(1) ¹	9.9082	10.5441	9.7205	9.9551	9.9472
Ce-O(1) ²	9.9082	10.5484	9.7243	9.9590	9.9551
Ce-O(1) ³	9.9082	10.5484	9.7243	9.9590	9.9551
Ce-O(2) ¹	10.2595	10.6302	10.4297	10.5784	10.5271
Ce-O(2) ²	10.2595	10.6302	10.4339	10.5827	10.5271
Ce-O(2) ³	10.2595	10.6302	10.4339	10.5827	10.5313
Ce-O(6) ¹	10.2227	10.7524	10.1780	10.4255	10.1983
Ce-O(6) ²	10.2268	10.7524	10.1821	10.4297	10.1983
Ce-O(6) ³	10.2268	10.7568	10.1821	10.4339	10.1983
Zr(Mg/Sb)1-O(4)×6	3.5771	3.4520	3.2100	3.3060	3.3154
Zr(Mg/Sb)2-O(3) ¹	3.4129	3.1367	3.7204	3.3695	3.6208
Zr(Mg/Sb)2-O(3) ²	3.4141	3.1378	3.7217	3.3707	3.6220
Zr(Mg/Sb)2-O(3) ³	3.4141	3.1389	3.7217	3.3713	3.6227
Zr(Mg/Sb)2-O(5) ¹	3.2311	3.3207	3.4093	3.3385	3.3462
Zr(Mg/Sb)2-O(5) ²	3.2317	3.3213	3.4099	3.3391	3.3468
Zr(Mg/Sb)2-O(5) ³	3.2329	3.3225	3.4111	3.3403	3.3486
Mo1-O(1)	-0.4301	-0.4225	-0.3783	-0.4680	-0.4165
Mo1-O(2)	-0.4291	-0.5177	-0.4839	-0.5425	-0.5469
Mo1-O(3)	-0.3452	-0.2125	-0.4307	-0.3026	-0.4310
Mo1-O(4)	-0.2809	-0.3092	-0.1553	-0.2657	-0.2909
Mo2-O(5)×2	-0.4184	-0.2128	-0.3333	-0.2607	-0.3772
Mo2-O(6)×2	-0.3890	-0.5212	-0.4097	-0.4791	-0.4099

Table 7

Mode	$\text{Ce}_2[\text{Zr}_{0.94}(\text{Mg}_{1/3}\text{Sb}_{2/3})_{0.06}]_3(\text{MoO}_4)_9$ $\epsilon_\infty=2.85$			
	ω_{oj}	ω_{pj}	γ_j	$\Delta\epsilon_j$
1	118.72	225.22	35.46	3.60
2	150.75	341.96	12.89	5.15
3	202.86	162.23	31.95	0.64
4	270.42	386.82	31.62	2.05
5	333.43	104.55	6.68	0.10
6	350.41	60.52	5.92	0.03
7	398.23	259.20	34.10	0.42
8	422.68	169.58	22.11	0.16
9	602.91	412.83	155.98	0.47
10	695.94	338.65	22.47	0.24
11	736.26	462.78	17.08	0.40
12	774.75	178.17	15.75	0.05
13	811.10	228.68	18.10	0.08
14	888.05	388.88	7.79	0.19
15	898.43	238.71	12.23	0.07
16	957.54	192.66	9.89	0.04